

# A Multi-Baseline 12 GHz Atmospheric Phase Interferometer with One Micron Path Length Sensitivity

Robert S. Kimberk<sup>1</sup>, Todd R. Hunter<sup>2</sup>, Patrick S. Leiker<sup>1</sup>, Raymond Blundell<sup>1</sup>, George U. Nystrom<sup>1</sup>, Glen R. Petitpas<sup>3</sup>, John Test<sup>1</sup>, Robert W. Wilson<sup>1</sup>, Paul Yamaguchi<sup>3</sup>, Kenneth H. Young<sup>1</sup>,

thunter@nrao.edu

## ABSTRACT

We have constructed a five station 12 GHz atmospheric phase interferometer (API) for the Submillimeter Array (SMA) located near the summit of Mauna Kea, Hawaii. Operating at the base of unoccupied SMA antenna pads, each station employs a commercial low noise mixing block coupled to a 0.7 m off-axis satellite dish which receives a broadband, white noise-like signal from a geostationary satellite. The signals are processed by an analog correlator to produce the phase delays between all pairs of stations with projected baselines ranging from 33–261 m. Each baseline’s amplitude and phase is measured continuously at a rate of 8 kHz, processed, averaged and output at 10 Hz. Further signal processing and data reduction is accomplished with a Linux computer, including the removal of the diurnal motion of the target satellite. The placement of the stations below ground level with an environmental shield combined with the use of low temperature coefficient, buried fiber optic cables provides excellent system stability. The sensitivity in terms of rms path length is 1.3 microns which corresponds to phase deviations of about  $1^\circ$  of phase at the highest operating frequency of the SMA. The two primary data products are: (1) standard deviations of observed phase over various time scales, and (2) phase structure functions. These real-time statistical data measured by the API in the direction of the satellite provide an estimate of the phase front distortion experienced by the concurrent SMA astronomical observations. The API data also play an important role, along with the local opacity measurements and weather predictions, in helping to plan the scheduling of science observations on the telescope.

## 1. Introduction

Astronomical radio and millimeter interferometers combine signals from multiple antennas in order to produce images of the sky. The signals must be combined with a predictable phase

---

<sup>1</sup>Harvard-Smithsonian Center for Astrophysics, 60 Garden Street, Cambridge, MA 02138

<sup>2</sup>National Radio Astronomy Observatory, 520 Edgemont Road, Charlottesville, VA, 22903

<sup>3</sup>Submillimeter Array, 645 North A’ohoku Place, Hilo, HI 96721

relationship based on the array geometry and the direction of the target field (Ryle & Hewish 1960). In the vacuum of space, the signal propagates from an astronomical source as a plane wave front. However, the atmosphere of the Earth is not a homogeneous transmission medium, and spatial and temporal variations in its constituents and properties along the line of sight distort the original plane wave front (Baars 1967). The resulting wave front aberration reduces the observed source visibility as compared to the true source visibility, a phenomenon often termed “radio seeing” (Baldwin 1990; Hargrave & Shaw 1978). If the variations become too large or too rapid, then they cannot be calibrated with the standard technique of phase referencing in which astronomical point sources are periodically observed to order to solve for the drift of each antenna’s complex gain vs. time (e.g. Carilli & Holdaway 1999; Wright 1996; Shapiro et al. 1979). In this situation, the data will often become unusable, especially on the longer baselines and at higher frequencies. Therefore, in order to survey potential sites for future interferometers and to promote optimal scheduling of observations in different frequency bands on an existing interferometer, it is desirable to construct an ancillary device to measure atmospheric phase variations on a continuous basis. Furthermore, these measurements should be performed on baseline lengths comparable to those of the existing (or planned) array configuration.

In this paper, we describe the design and operation of a novel, broadband, multi-baseline atmospheric phase interferometer (API) operating at the Submillimeter Array (SMA)<sup>1</sup> telescope site located near the summit of Mauna Kea, Hawaii. There are many examples of previous and currently operating instruments that correlate geostationary satellite beacon signals at astronomical observatory sites (Middelberg et al. 2006; Hiriart et al. 2002; Radford et al. 1996; Ishiguro et al. 1990; Masson et al. 1990) and elsewhere (Kirkland et al. 2000; Shao et al. 1999). In contrast, rather than using a beacon tone, our instrument correlates broadband digital television emission from satellites which contains far more power than the beacon tones, thereby enabling a high signal to noise ratio while avoiding the many drawbacks of a very narrow bandpass filter. The use of the transponder signal rather than the satellite beacon to measure the atmospheric phase is derived from the Berkeley Illinois Maryland Array (BIMA) phase monitor design (Lay 1998b). In addition to higher signal to noise, the broadband system eliminates the possibility of signal loss due to frequency drifts of the beacon tone that can exceed the bandwidth of the narrow band filters required in beacon detection systems. The API acronym which we adopt in this paper for our system is synonymous with the term Radio Seeing Monitor adopted by Ishiguro et al. (1994).

---

<sup>1</sup>The Submillimeter Array (SMA) is a collaborative project between the Smithsonian Astrophysical Observatory and the Academia Sinica Institute of Astronomy & Astrophysics of Taiwan.

## 2. Instrument

### 2.1. Theory of operation

In the presence of a Gaussian distribution of atmospheric phase distortions with standard deviation  $\sigma$  (in radians at the observing frequency), the observed visibility function of a celestial source is reduced by an exponential factor:  $V_{\text{obs}} = V_{\text{src}} \exp(-\sigma^2/2)$  (Thompson et al. 2001). At submillimeter wavelengths, the dominant atmospheric effect on the incoming wave front is due to variations in tropospheric water vapor. The total precipitable water vapor (PWV) toward the zenith above good sites for (sub)millimeter astronomy typically ranges from  $< 1$  to several millimeters. For reference, a variation of 0.1 mm PWV produces a 0.645 mm path length difference (Shao et al. 1999; Lay 1998a), resulting in a phase change of 4.0 radians at 300 GHz. Fortunately, at microwave and submillimeter wavelengths, the index of refraction of water vapor is independent of frequency, except near strong absorption lines (Thompson et al. 2001). As a consequence, the atmosphere is mostly non-dispersive, allowing one to extrapolate the phase front deviations ( $\sigma_{\text{cm}}$ ) measured at a low (centimeter wavelength) frequency ( $\nu_{\text{cm}}$ ) into predicted phase deviations ( $\sigma_{\text{submm}}$ ) at submillimeter observing frequencies ( $\nu_{\text{submm}}$ ) by a simple ratio:  $\sigma_{\text{submm}} = \sigma_{\text{cm}}(\nu_{\text{submm}}/\nu_{\text{cm}})$ . With a typical down-link frequency range of 11.7–12.7 GHz, K<sub>u</sub> band satellite digital television transmissions provide a convenient strong signal with which to probe the tropospheric path variations. We wish to predict the phase deviations to an accuracy of  $1^\circ$  at 700 GHz, the highest frequency of operation of the SMA (Hunter et al. 2005). In order to achieve this performance using a 12 GHz API requires an rms noise level of  $\sim 3.5 \times 10^{-4}$  radians.

### 2.2. Description

The new API for the SMA is a multi-element 12 GHz interferometer that observes a geostationary satellite. A block diagram of the system is shown in Figure 1. Each station consists of an inexpensive (\$65) low noise mixing block (LNB) designed for satellite TV reception coupled to a 0.7m diameter off-axis parabolic dish antenna via a scalar feedhorn. The LNB contains a low noise amplifier with a rated noise temperature of 30 K (Invacom QPH-081), and we measured the total receiver temperature to be 70 K. We modified each LNB to accept an external local oscillator (LO) signal coupled into a toroidal dielectric resonator on the circuit board.<sup>2</sup> The LNB can simultaneously receive two linearly polarized transponder bands and two circularly polarized transponder bands. Separation is achieved by an orthomode transducer, and we use the intermediate frequency (IF) signal from one of the circular polarizations. The digital quadrature phase modulated signal transmitted by the satellite is spectrally white. The API’s correlation of a white noise signal has

---

<sup>2</sup>Larry D’Addario of JPL developed a lower loss technique for injecting the LO into the LNB while adapting the SMA API design for use by NASA’s Deep Space Network and as a site testing instrument for the Square Kilometer Array (SKA).

the benefit of eliminating any spurious multipath effects (Rogers et al. 1993). A white noise source of 60 MHz bandwidth will decorrelate in  $\sim 5$  m of path difference so only objects closer than that distance can potentially reflect an interfering signal. However, the white noise correlation does impose the need to equalize the delays from each antenna to the correlator with spools of optical fiber. A pair of assembled stations with their NEMA enclosures is shown in Figure 2 along with the central electronics rack. Each station requires only 50 W of A/C power.

The SMA site occasionally experiences significant periods of snow, ice and high winds, which present a challenge for deploying sensitive equipment. However, because the SMA consists of 24 pads and 8 antennas, two thirds of the pads are unoccupied at any given time. The idea of installing the API equipment in the pits of the unused pads was conceived by former site director Antony Schinckel. The underground space containing the API antenna is hidden from view by an environmental cover made from 19 mm thick marine grade high density polyethylene. The cover prevents wind buffeting of the antennas, a potential problem as the system is sensitive to micrometer scale physical displacement of the antennas. A photo of the dish antenna and associated electronics box installed into an SMA pad is shown in Figure 3. The station geometry of the API is listed in Table 1, including the pad numbers, the baseline lengths ( $B_{total}$ ) and the projected lengths of the baselines ( $B_{proj}$ ) as viewed from the target satellite. A topographical map of the SMA site with the pad locations indicated can be found in Ho, Moran, & Lo (2004), while further details of the SMA technical design, digital phase-locked loops, and overall LO phase stability can be found in Blundell (2007), Hunter et al. (2011), and Kubo et al. (2006), respectively.

Each of the antenna’s electronics is connected via two 1330 nm single-mode fiber optic cables to the equipment rack in the SMA fiber patch panel vault located underground adjacent to the SMA control building. The rack distributes the common LO signal on one fiber and collects the intermediate frequency (IF) signals from the other fiber. These fibers are two of the three available fibers that can be used to carry the submillimeter receiver LO and IF signals when an SMA antenna is present on the pad. The use of these buried fiber cables (which were custom designed to have a low phase vs. temperature coefficient) combined with the placement of the central electronics in an underground room promotes a phase-stable system by effectively eliminating phase drifts due to diurnal temperature swings. The IF signals from each station are processed as pairs on ten “baseline boards”. Each board contains a CMOS analog switch driving the IF port of a mixer which applies an alternating  $180^\circ$  phase shift to one of the two station signals. The signal enters the RF port of the mixer and emerges from the LO port before proceeding to the analog correlator. This Walsh pattern modulation (Granlund, Thompson, & Clark 1978) removes the  $1/f$  noise (drift) of the correlator’s Gilbert cell multipliers, following the example of the BIMA phase monitor (Lay 1998b). The IF signal pairs are processed into in-phase ( $I$ ) and quadrature ( $Q$ ) outputs by the correlator which is a broadband direct conversion quadrature ( $I/Q$ ) demodulator (Analog Devices AD8347) commonly used in digital satellite television receivers. These baseline pair outputs are digitized at a rate of 8 kHz by an analog to digital converter card on the PCI bus of a dedicated Linux computer. The baseline phases and amplitudes are calculated from  $\arctan(Q/I)$  and  $\sqrt{Q^2 + I^2}$ , respectively.

The Walsh demodulation is performed in software by the API computer control program, which subsequently averages the data to 10 Hz.

### 2.3. Satellite target and sensitivity

The satellite we have chosen to observe is Ciel 2 (NORAD 33453). This Canadian satellite is a Spacebus-4000C4 model launched in 2008 and currently operating at 129° West geostationary orbit position. From Mauna Kea, it appears at an azimuth of 124° and an elevation of 52° which is sufficiently high to avoid vignetting of the beam by the cylindrical wall of the concrete pad. The equivalent isotropic radiated power (EIRP) is 52 dBW in each of its 30 MHz transponder bands. A spectrum analyzer trace showing the satellite signal bands at 12.4 GHz used by the API correlator is shown in Figure 4. The signal to noise ratio ( $SNR$ ) of the received satellite signal power is about 8 dB, which places the API system in the “strong source” case when considering the sensitivity. For our purposes, we are interested in the theoretical noise floor of the API with respect to the measured fringe phase angle. We consider the real signal and noise voltages from two antennas to be  $S_1(t)$ ,  $S_2(t)$ ,  $N_1(t)$ , and  $N_2(t)$ . With the delay set such that the satellite is at the center of the white light fringe,  $S_1(t) = S_2(t) \equiv S(t)$ . Consequently, the  $I$  output from the  $I/Q$  demodulator will be proportional to  $(\langle S(t) \rangle_{\text{rms}})^2 \equiv S_{\text{rms}}^2$  because only this term integrates coherently and the other terms will be small. In the  $Q$  output, the  $S_{\text{rms}}^2$  term will integrate to zero due to the 90° phase shift, thus we are left with the sum of the cross terms and the noise product term. Since  $(\langle N_1 \rangle_{\text{rms}})^2 \approx (\langle N_2 \rangle_{\text{rms}})^2 \equiv N_{\text{rms}}^2$ , the rms deviation of  $Q$  from zero will follow the radiometer equation for the case of identical receivers and antennas (see Eq. 7-32 of Crane & Napier (1989)). Therefore, we can relate the theoretical rms noise floor of the API in terms of the rms fringe phase angle,  $\sigma_{\text{rms}}$  (in radians), to the  $SNR$ , the received bandwidth ( $B$ ), and the integration time ( $\tau$ ) by starting with the small angle approximation:

$$\sigma_{\text{rms}} = \langle \arctan(Q/I) \rangle_{\text{rms}} \approx Q_{\text{rms}}/I = \frac{\sqrt{(2S_{\text{rms}}^2 N_{\text{rms}}^2 + N_{\text{rms}}^4)/(B\tau)}}{S_{\text{rms}}^2} = \sqrt{\frac{2/SNR + 1/SNR^2}{B\tau}}. \quad (1)$$

In cases such as ours where the  $SNR$  is large, a further approximation can be made:

$$\sigma_{\text{rms}} \approx \sqrt{\frac{2/SNR}{B\tau}}, \quad (2)$$

which is different from the approximation applied in the more typical, “weak source” radio astronomy case. With the current operating parameters of  $B = 60 \times 10^6$  Hz, and  $t = 0.1$  s, the theoretical noise floor is  $1.3 \times 10^{-4}$  radians or  $0.013^\circ$  at 12.4 GHz. The practical noise level achieved in the laboratory,  $0.02^\circ$  rms, is only about 50% worse than this prediction. At 700 GHz, the measured noise corresponds to an rms noise floor of  $0.73^\circ$  phase, which meets the requirement.

## 2.4. Data products

Because geostationary satellites cannot maintain a perfectly circular orbit exactly in the equatorial plane, they typically exhibit a small apparent diurnal motion when viewed from the Earth. This motion amounts to several turns of phase on our baselines. We remove this effect in real time by automatically computing a running sinusoidal least-squares fit to the phase data. The standard deviation of the phase on each baseline is then computed for a series of time scales ranging from 1 to 2048 seconds in powers of two. The square root of the phase structure function (Tatarski 1961) is also computed using these same time scales plus the additional lags of 768, 1536, and 2816 seconds. The processed data are then written to the SMA distributed shared memory (DSM) system, which allows them to be displayed on the operator’s monitor screens and automatically written to the central engineering data archive. The cross-correlation amplitudes from each baseline and the auto-correlation amplitudes from each station are also produced by the demodulators as voltage outputs which are sampled, copied to DSM, and stored to the engineering data archive. These amplitude values can alert the operators to the presence of water or snow on the environmental shield as it can substantially (or completely) attenuate the satellite signal. When necessary, functionality can then be restored by sweeping the shields clear.

## 2.5. Calibration of the I/Q demodulator

After the initial mechanical attachment and manual alignment of the dish antennas in each pad, the instrument requires very little in terms of calibration. We did find that the  $I/Q$  demodulators exhibit a small difference in the complex gain between their two output channels. Because of the satellite’s diurnal motion, this imbalance leads to a predictable pattern in the cross-correlation amplitude vs. time, typically about 5% in terms of the peak to peak variation with  $\approx 0.5$ –3 dozen periods per day, depending on the baseline length. We performed a least-squares fit to this pattern over several days of data from each baseline and derived the appropriate software gain factors for each demodulator in order to bring the outputs into agreement. After applying these gain factors to the digitized voltages in software, a large fraction of the amplitude pattern is eliminated (Figure 5).

## 3. Results

The first three API stations were installed in late 2009, the fourth in July 2010, and the fifth and final station in July 2011. In this section, we present preliminary results from a two month period from November 1 through December 31, 2011 during which the SMA was in compact configuration, enabling all stations to see the sky simultaneously. Nine of the ten baseline boards were functioning properly throughout this period. Baseline 4-5 had consistently low correlated amplitude due to a fiber delay error, so those data are ignored in the following analysis. The delay error was corrected on January 11, 2012.

### 3.1. Examples of variable atmospheric conditions in the API data

The rms phase from two selected baselines of the API (the shortest and longest) over a one week period is shown in Figure 6. The well-known diurnal cycle of good phase stability above Mauna Kea at night and poor stability during the day (Masson 1994a) is clearly evident in the data. One can also see that on some nights the atmosphere is significantly more stable than on others. The data from the different baselines behave similarly but not identically, which is expected given the different baseline lengths and orientations and the nature of water vapor fluctuations. The rms is generally worse on longer baselines but by varying amounts. Detailed comparisons of the variation in the rms phase measured by the API with the SMA interferometer phase stability measured on calibrators typically show excellent agreement. To illustrate this agreement quantitatively, we continuously observed a strong quasar with the SMA in compact configuration over a two hour interval during which the observing conditions improved drastically. Figure 7 compares the 32-second time scale root phase structure function from the shortest API baseline with the 230 GHz phase recorded at 30 second integrations from each SMA baseline. The median of the per-baseline standard deviations of the 230 GHz phases dropped by a factor of 9.5, from  $103^\circ$  during the 03:30-04:00 period to  $10.6^\circ$  during the 04:30-05:00 period. Over these same periods, the standard deviation of the API root phase structure function dropped by a factor of 9.7, from  $2.18^\circ$  to  $0.23^\circ$ . This agreement demonstrates that the API data provide a full-time, direct assessment of the submillimeter observing conditions on Mauna Kea for comparable interferometric baselines.

### 3.2. Comparison of rms phase among the API baselines

The cumulative distribution function of the rms path length on a 64 second timescale is shown in Figure 8 for all nine API baselines corrected to the zenith by dividing by  $\sqrt{\sec(\text{zenith angle})}$  (Coulman 1985). There is an extended tail in the distribution toward higher values at all timescales, reflecting the worst observing conditions on Mauna Kea. Therefore, rather than using the mean and standard deviation, we compute the median and median absolute deviation (MAD) for the zenith-corrected rms path length in order to better represent the variation in the majority of the data. Listed in Table 3 are the results for the 512 second timescale which provides an estimate of the median rms phase variation between typical visits to a phase calibrator during a science observation. Considering that the medians are derived from only two months of data, the nighttime values agree well with the overall nighttime median value of  $101\mu\text{m}$  for Mauna Kea measured over 1406 days from 1990-1998 with the original SAO 100 m baseline phase monitor (Moran 1998). For our calculations, “nighttime” is an approximate term that refers to the period of time from sunset plus two hours to sunrise plus two hours, and is quite similar to the definition used by Moran (1998) of 20 hours to 8 hours local time for this tropical location. Finally, the smaller values of both the median and the MAD found during nighttime are further indication of the diurnal effect.

### 3.3. Root phase structure function slope and corner time

Each baseline of the API provides an independent measurement of the root phase structure function. For each baseline, we have fit the slope ( $\alpha$ ) and corner time ( $t_{\text{corner}}$ ) of the root phase structure function for each time interval following the iterative procedure of Holdaway et al. (1995). To find the initial slope, we perform a linear least squares fit to the first six data points (lags of 1-32 seconds). We derive the initial corner time by computing median value of the structure function over the longer lags (beginning at 64 seconds) and find the time where the linear fit crosses this value. This process is repeated until convergence, which requires at most a few iterations. The median and MAD values of  $\alpha$  and  $t_{\text{corner}}$  per baseline over the two month period are listed in Table 3. The histogram of values of  $\alpha$  for the shortest and longest baselines and a cumulative distribution function (CDF) for all nine baselines are shown in Figures 9 and 10. In this table and figures, we have excluded data from the time intervals when any of the baselines reported abnormally low normal amplitudes, that is, when one or more of the pad covers were blanketed with snow. As seen with the previous SAO instrument on Mauna Kea (Masson 1994a),  $\alpha$  varies over a range of values (0.2-0.8). The median value of  $\sim 0.65$  is intermediate between the expected Kolmogorov exponent for a thick atmosphere (0.83) and a thin atmosphere (0.33) (Thompson et al. 2001). The relatively small values of the MAD demonstrate that this intermediate value of  $\alpha$  is persistent, and does not represent a time average between the two extreme cases. In fact, intermediate values for  $\alpha$  of  $\sim 0.7$  are seen at many other astronomical telescope sites (Masson 1994b). The corner times of  $\sim 200$  sec correspond to a flattening of the frequency spectrum of phase variations below  $\sim 0.005$  Hz, but with a fairly large variation. Again, this result is consistent with the conclusions from the previous SAO phase monitor on Mauna Kea. Finally, we note that the shapes of the histograms and CDFs are very similar to those derived for the ALMA site from the NRAO site test interferometer (Holdaway et al. 1995; ALMA science portal 2012).

### 3.4. Practical usage of the API

During each six-month semester, the SMA normally cycles through four configurations ranging from sub-compact to very-extended (Petitpas et al. 2010). The range of baselines is given in Table 2. In the extended configurations, some of the API antennas are covered by SMA antennas; however, in all cases at least three API baselines are operational with projected lengths ranging from 33 m to at least 129 m. The API data have become a useful tool for the observatory’s science operations team. The long term use of the API continues to emphasize the fact that the phase stability is generally worse during the day and better at night. For this reason, the SMA typically executes science projects from very late afternoon until some number of hours after sunrise (Christensen et al. 2008). The superior nighttime phase stability generally persists for some period after sunrise (see Fig 6), but the length of this period is quite variable. However, the deterioration in phase stability is easily seen in the API data, and by watching it closely, the current science observation can be curtailed when necessary by acquiring the remaining calibration observations before the conditions



become unusable. Unfortunately, the degree to which the day vs. night phase stability dichotomy holds true does not seem to be correlated with any other better studied atmospheric variables such as PWV (see also Masson (1994a)), relative humidity, etc. Therefore, the use of the API as a predictive tool for scheduling upcoming science observations is limited, and those decisions are still generally dominated by the PWV forecast.

In addition to tracking the diurnal conditions, the API data helps to alert the operations team to the passage of major weather patterns. For example, after just a few months of use, it became clear that poor phase stability was almost always assured when the forecast predicted a transition from very dry to very wet conditions. It is also occasionally true that transitions from very wet to very dry conditions also result in poor phase, but not always (in contrast to the case for the reverse trend). Therefore, if we are expecting half of the night to be wet (or dry) changing to dry (or wet), it is almost always prudent to schedule a lower frequency project, because even if the opacity improves, one can expect the phase to remain unstable for longer. Finally, we do occasionally see long term trends of poor phase stability at night, typically when there is a lot of moist air moving across the Hawaiian Islands. During these periods, we tend to preferentially schedule lower frequency projects since they are less affected by poor phase stability than the higher frequency projects and have a greater chance of success. We can then monitor the API data during the day to watch for improvements in phase stability which could suggest that it is worth trying higher frequency observations that evening.

#### 4. Summary

We have successfully developed and deployed a five-station 12 GHz API for the SMA. Each of the ten baselines correlates a broadband digital signal from a geostationary television broadcast satellite. The stations are installed in the covered pits of SMA antenna pads, protecting them from environmental disturbances, and yielding a path length sensitivity of  $\approx 1$  micron. The real-time phase stability data correlates well with the observed phase stability of the SMA interferometer data stream. Preliminary statistics on the rms path length and the behavior of the root phase structure function (slope and corner time) are consistent with the previous single baseline atmospheric phase monitor experiment on Mauna Kea. The SMA API is used regularly along with other measurements of weather conditions and forecasts to schedule science observations in appropriate conditions for the desired frequency band, and to help ensure that these observations are completed successfully. Future studies of the phase stability statistics for Mauna Kea will become possible as the archive of API data grows.

We thank John Kovac for assistance in the measurement of the receiver temperature of the LNB, and Jim Moran for useful discussions. The National Radio Astronomy Observatory is a facility of the National Science Foundation operated under cooperative agreement by Associated Universities, Inc. This research has made use of NASA's Astrophysics Data System Bibliographic

Services. The authors extend special thanks to those of Hawaiian ancestry on whose sacred mountain we are privileged to be guests.

## REFERENCES

- ALMA Science portal, 2012, <https://almascience.nrao.edu/about-almawhether/overview>
- Baars, J. 1967, IEEE Transactions on Antennas and Propagation, 15, 582
- Baldwin, J. E., 1990, URSI/IAU Symposium on Radio Astronomical Seeing, 1
- Blundell, R. 2007, IEEE/MTT-S International Microwave Symposium, 2007, p. 1857-1860, 1857
- Carilli, C. L., & Holdaway, M. A. 1999, Radio Science, 34, 817
- Christensen, R. D., Kubo, D. Y., & Rao, R. 2008, Proc. SPIE, 7016, 701608-1
- Coulman, C. E. 1985, ARA&A, 23, 19
- Crane, P. C., & Napier, P. J. 1989, Synthesis Imaging in Radio Astronomy, 6, 139
- Granlund, J., Thompson, A. R., & Clark, B. G. 1978, IEEE Transactions on Electromagnetic Compatibility, 20, 451
- Hargrave, P. J., & Shaw, L. J. 1978, MNRAS, 182, 233
- Hiriart, D., Valdez, J., Zaca, P., & Medina, J. L. 2002, PASP, 114, 1150
- Ho, P. T. P., Moran, J. M., & Lo, K. Y. 2004, ApJ, 616, L1
- Hogg, D. E. 1992, Millimeter Array Memo 79, NRAO
- Holdaway, M., Radford, S., Owen, F. & Foster, S., 1995, ALMA Memo 129, <http://www.alma.nrao.edu/memos/html-memos/abstracts/abs129.html>
- Hunter, T. R., Kimberk, R., Leiker, P. S., Tong, C.-Y. E., & Wilson, R. W. 2011, arXiv:1101.1506
- Hunter, T. R., Barrett, J. W., Blundell, R., et al. 2005, Sixteenth International Symposium on Space Terahertz Technology, 58
- Ishiguro, M., Kanzawa, T., & Kasuga, T. 1990, URSI/IAU Symposium on Radio Astronomical Seeing, 60
- Ishiguro, M., Kawabe, R., Nakai, N., Morita, K.-I., Okumura, S. K., & Ohashi, N. 1994, IAU Colloq. 140: Astronomy with Millimeter and Submillimeter Wave Interferometry, 59, 405
- Kirkland, M. W., Carlos, R., Shao, X.-M., Dehaven, X. V., & Jacobson, A. R. 2000, IEEE Transactions on Geoscience and Remote Sensing, 38, 849

- Kubo, D. Y., Hunter, T. R., Christensen, R. D., & Yamaguchi, P. I. 2006, Proc. SPIE, 6275, 62751Y
- Lay, O. P. 1998, MMA Memo #209, <http://www.alma.nrao.edu/memos/html-memos/abstracts/abs209.html>
- Lay, O. P. 1998, BIMA Memo 72, <http://bima.astro.umd.edu/memo/memo72/help.html>
- Masson, C. R. 1994a, IAU Colloq. 140: Astronomy with Millimeter and Submillimeter Wave Interferometry, 59, 87
- Masson, C. R. 1994b, IAU Colloq. 158: Very High Angular Resolution Imaging, 1
- Masson, C., Williams, J. D., Oberlander, D., & Hernstein, J. 1990, SMA Technical Memorandum #30, <http://www.cfa.harvard.edu/sma/memos/30.pdf>
- Middelberg, E., Sault, R. J., & Kesteven, M. J. 2006, PASA, 23, 147
- Moran, J. M. 1998, Proc. SPIE, 3357, 208
- Petitpas, G., Zhang, Q., Katz, C., Patel, N., & Blundell, R. 2010, Proc. SPIE, 7737, 77370X
- Radford, S. J. E., Reiland, G., & Shillue, B. 1996, PASP, 108, 441
- Rogers, A. E. E., Barvainis, R., Charpentier, P. J., & Corey, B. E. 1993, IEEE Transactions on Antennas and Propagation, 41, 77
- Ryle, M., & Hewish, A. 1960, MNRAS, 120, 220
- Shao, X. M., Carlos, R. C., Kirkland, M. W., Kao, C.-Y. J., & Jacobson, A. R. 1999, J. Geophys. Res., 104, 16729
- Shapiro, I. I., et al. 1979, AJ, 84, 1459
- Tatarski, V. I., 1961, Wave Propagation in a Turbulent Medium, McGraw-Hill, New York
- Thompson, A. R., Moran, J. M., & Swenson, G. W., Jr. 2001, Interferometry and synthesis in radio astronomy, 2nd ed., Wiley , New York
- Wright, M. C. H. 1996, PASP, 108, 520

Table 1: Stations and baseline lengths in the SMA API.

Stations	Baseline	Baseline length (m)		Pad height difference (m)	Azimuth (°)	Blocked in configuration <sup>a</sup>
	pads	$B_{\text{total}}$	$B_{\text{proj}}$			
1-2	22-10	46	33	6.7	143/323	–
2-3	10-14	134	123	4.8	72/252	ext
3-1	14-22	156	129	11.4	88/268	ext
4-1	15-22	158	118	11.8	134/314	ext
3-4	14-15	124	122	0.3	20/200	ext
2-4	10-15	114	86	5.1	131/311	ext
2-5	10-18	299	248	18.0	90/270	vex
3-5	14-18	176	135	13.2	103/283	vex
4-5	15-18	227	206	12.9	70/250	vex
5-1	18-22	328	261	24.7	96/276	vex

<sup>a</sup>In extended and very-extended configurations, some of the baselines are blocked by SMA antennas. Baseline 1-2 is never blocked because pads 10 and 22 are never occupied by SMA antennas in the standard sequence of configurations.

Table 2: Baseline lengths of SMA and API during the various SMA configurations

Configuration of SMA	Range of SMA baselines (m)	Number of stations	Range of API baselines (m) <sup>a</sup>
sub-compact	9.5-69	5	33-261
compact	17-77	5	33-261
compact-north	17-139	5	33-261
extended	44-227	3	33-261
very-extended	68-508	4	33-129

<sup>a</sup>Projected baseline lengths perpendicular to the target satellite direction

Table 3: Median and median absolute deviation (MAD) of  $\alpha$ ,  $t_{\text{corner}}$ , and rms path length for nine API baselines

Baseline (pads)	Length (m) $B_{\text{proj}}$	$\alpha$ Median (MAD)	$t_{\text{corner}}$ (sec) Median (MAD)	rms path length (microns) <sup>a</sup>	
				24-hour Median (MAD)	Nighttime <sup>b</sup> Median (MAD)
22-10	33	0.63 (0.07)	92 (35)	73 (38)	60 (28)
10-14	86	0.69 (0.03)	155 (68)	127 (71)	104 (51)
14-22	118	0.66 (0.04)	193 (95)	145 (82)	119 (59)
15-22	122	0.61 (0.06)	203 (101)	135 (73)	111 (52)
14-15	123	0.60 (0.06)	221 (109)	144 (81)	118 (57)
10-15	129	0.59 (0.06)	246 (123)	150 (85)	122 (60)
18-22	135	0.53 (0.08)	299 (142)	153 (87)	126 (62)
14-18	248	0.59 (0.05)	359 (175)	193 (108)	160 (78)
15-18	261	0.62 (0.04)	347 (170)	198 (110)	163 (79)

<sup>a</sup>Calculated over 512 second intervals and corrected to the zenith.

<sup>b</sup>Nighttime is defined as sunset plus 2 hours to sunrise plus 2 hours.

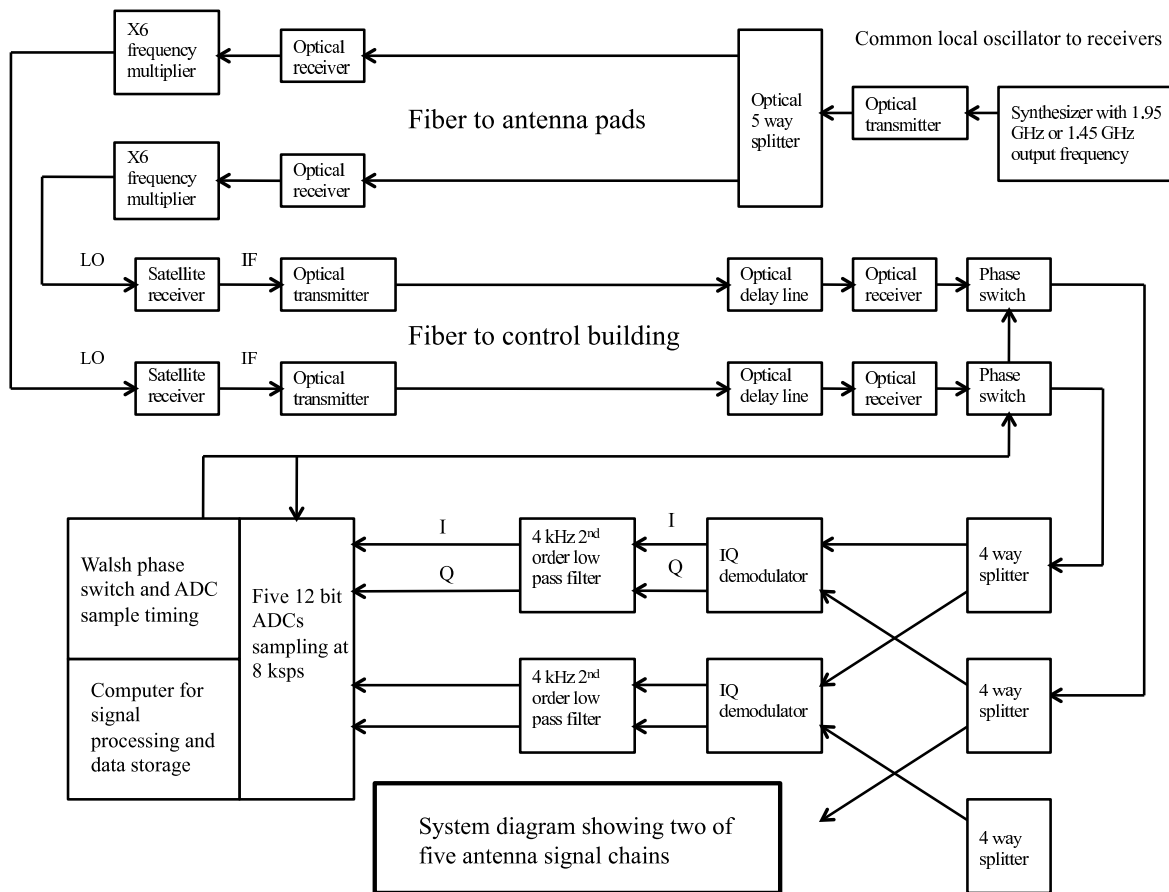


Fig. 1.— Block diagram for two stations of the API and the associated IF electronics.



Fig. 2.— Photograph of two stations of the SMA API and the central electronics rack during laboratory testing. The triangular base frame is bolted to the concrete floor of the SMA antenna pad.

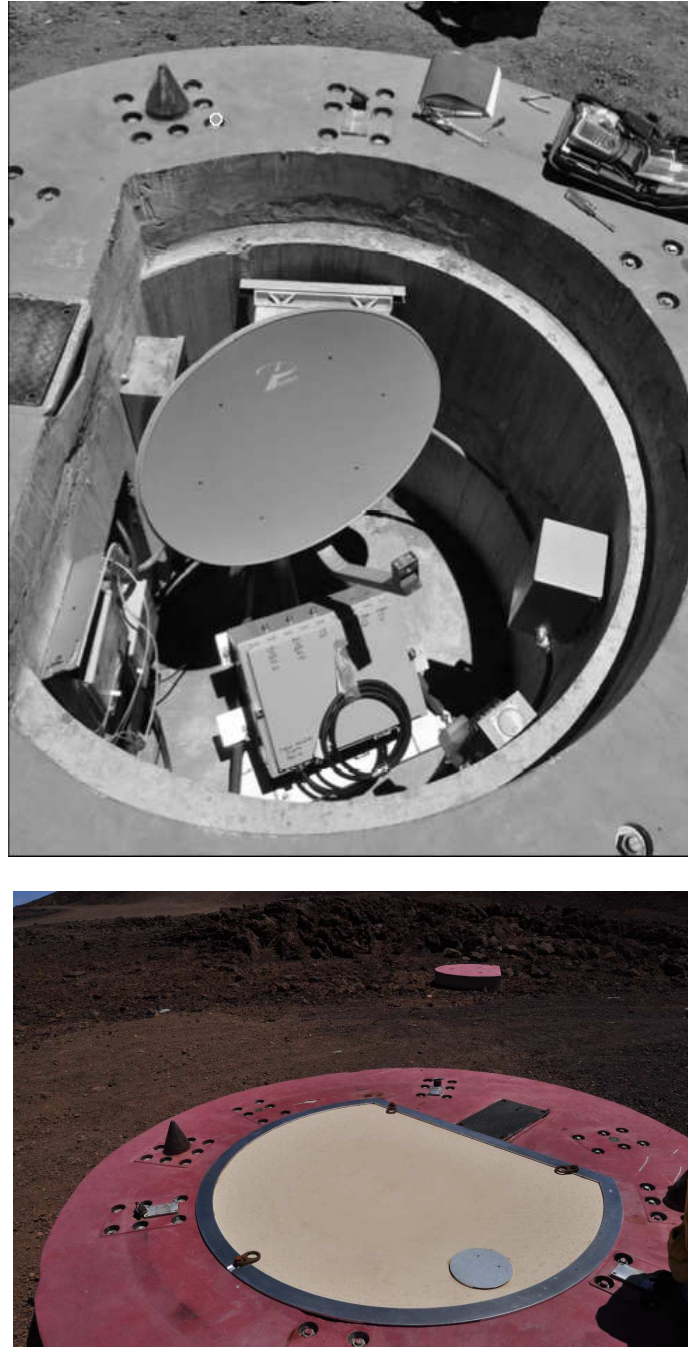


Fig. 3.— Photographs of one station of the SMA API installed into a pad: (upper panel) with cover removed; (lower panel) with cover in place. The short chimney provides ventilation by a small fan.



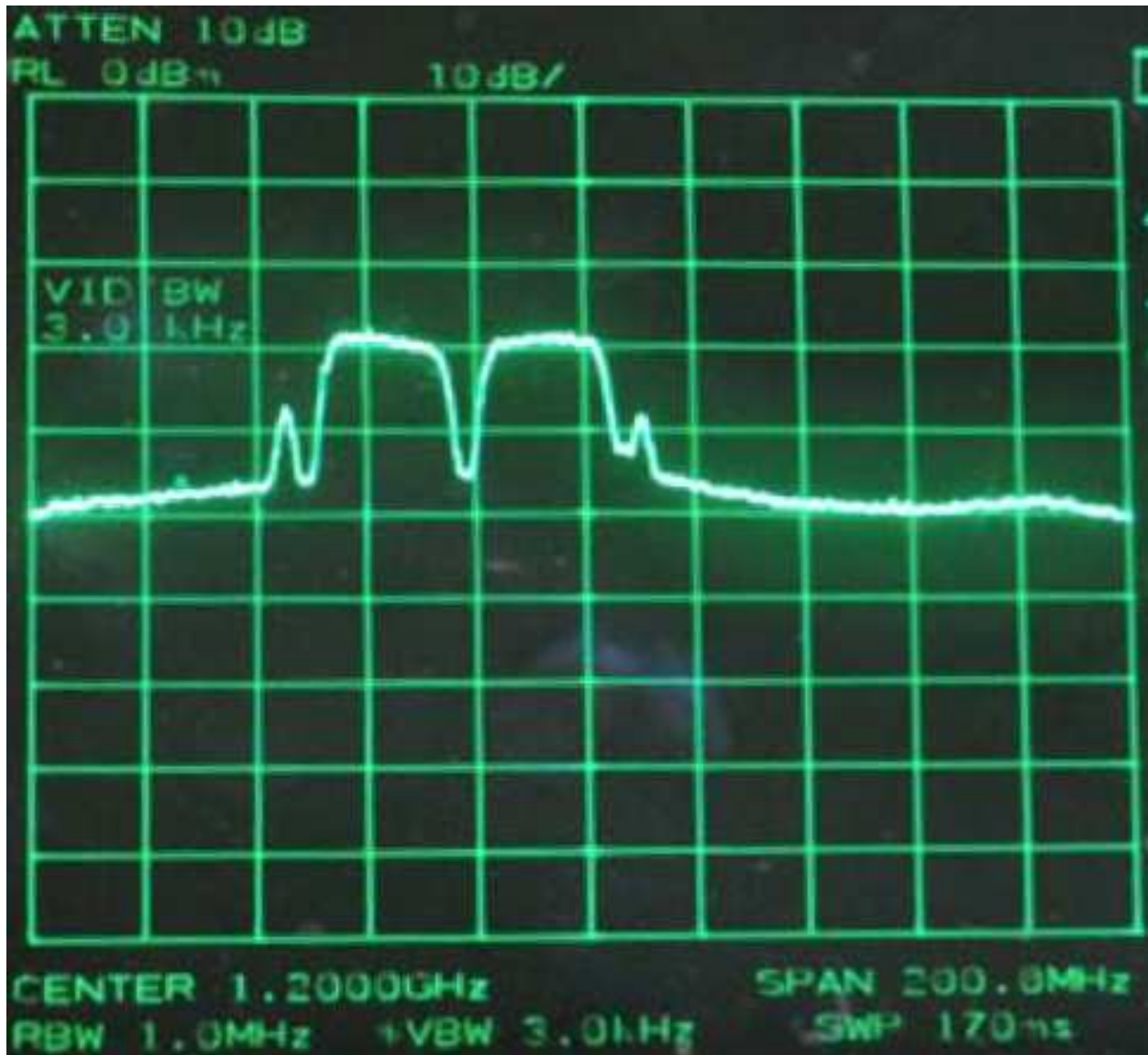


Fig. 4.— Spectrum analyzer trace of the IF output of one station of the API with the dish antenna pointed at the satellite Ciel-2. In this case, the signal power to noise power ratio exceeds 10 dB, but the typical value is  $\geq 8$  dB.

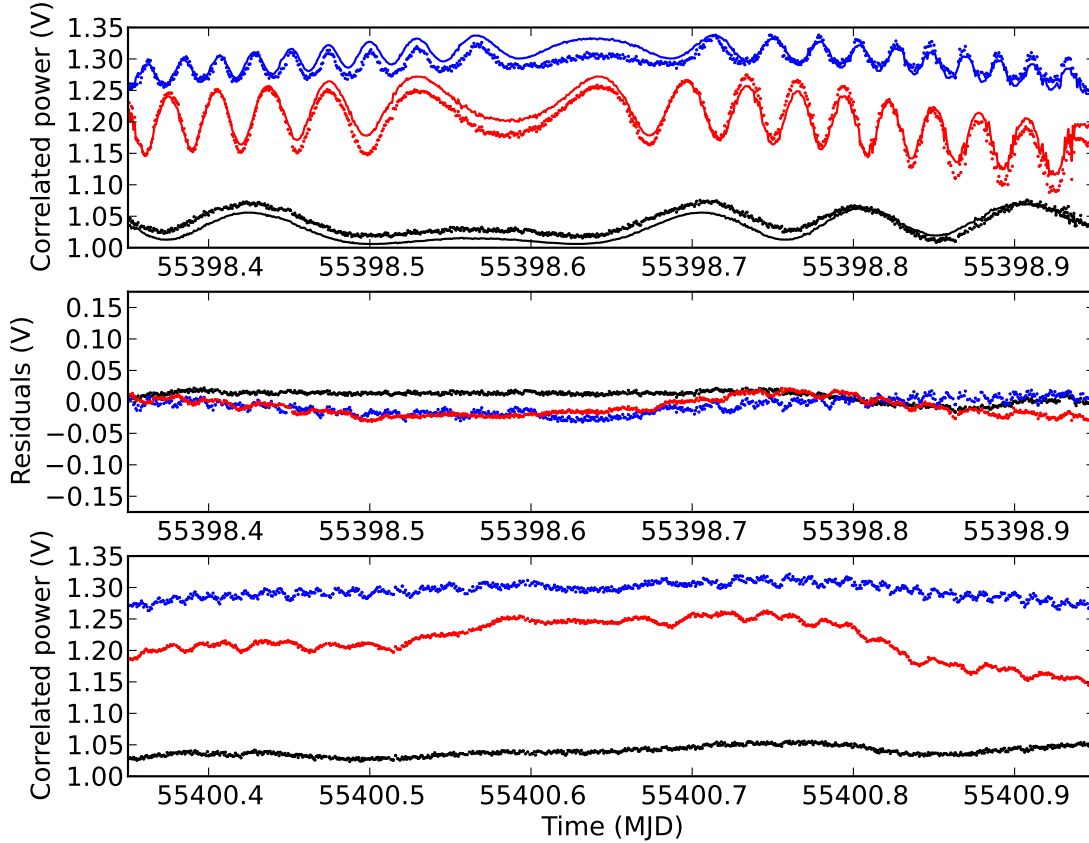


Fig. 5.— The baseline correlated power vs. time for three API baselines. Dots are the measurements and lines are the model fits for the relative gains of the  $I/Q$  demodulator outputs. Panel (a) shows the raw data with the model fit overlaid, from top to bottom the data are from baselines: 2–4 ( $B_{\text{proj}} = 86\text{m}$ ), 3–4 (122m), and 1–2 (33m). Panel (b) shows the residuals after model subtraction. Panel (c) shows the raw data from two days later, after the model coefficients were installed into the software. The high frequency variation is mostly eliminated.

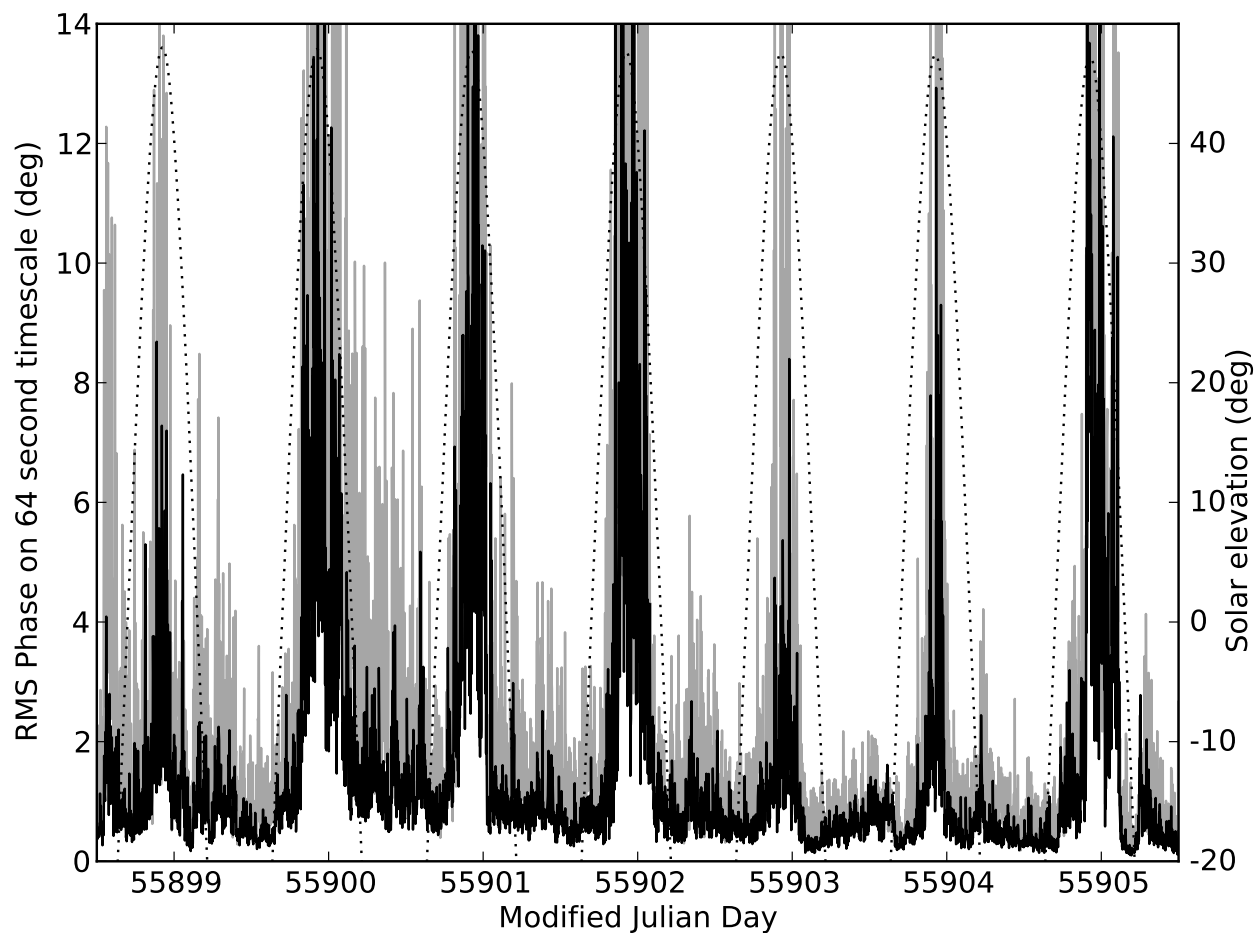


Fig. 6.— The rms phase at 12.4 GHz on 64-second intervals measured on two different baselines (black line: shortest baseline ( $B_{\text{proj}} = 33$  m), gray line: longest baseline ( $B_{\text{proj}} = 261$  m) over a one week period in early December 2011. The dotted line is the elevation of the sun, as specified on the right side y-axis. The diurnal cycle of lower and more stable rms phase at nighttime is clearly evident.

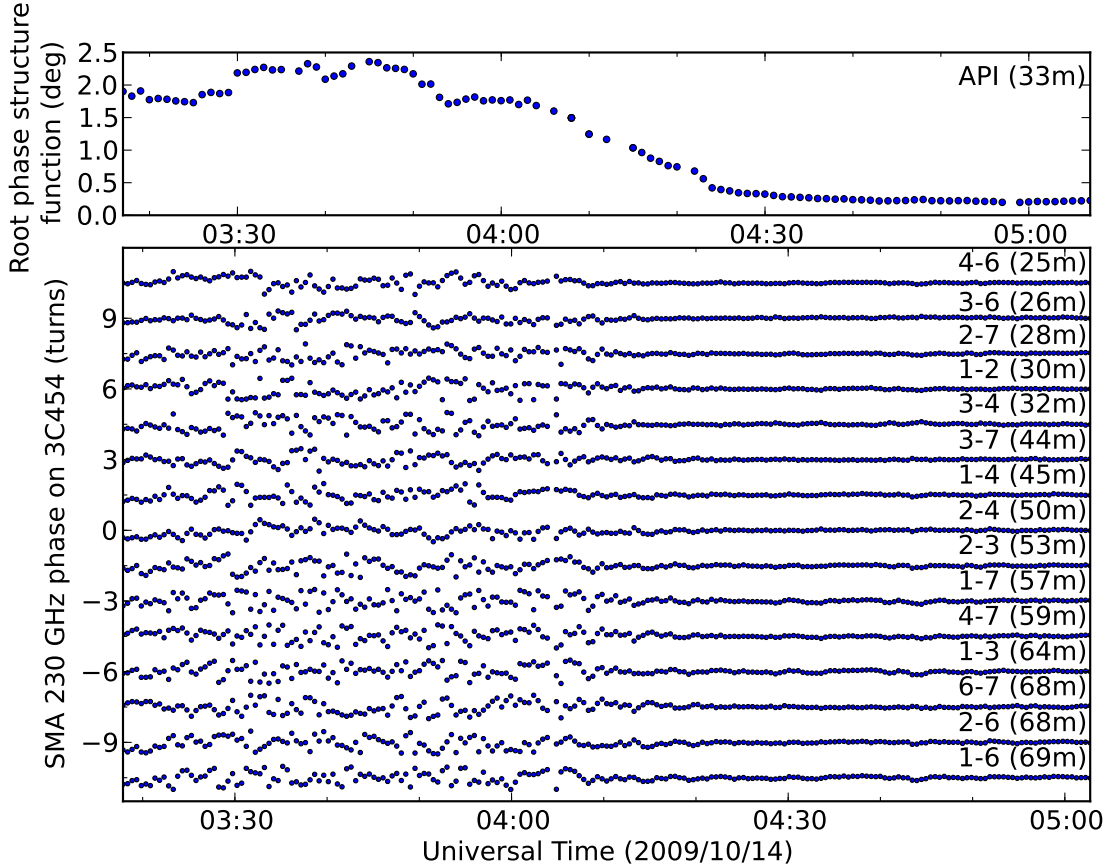


Fig. 7.— Top panel: The 32 second root phase structure function from the shortest API baseline. Bottom panel: The calibrated SMA interferometer phase recorded on 15 baselines while observing the bright quasar 3C454 with a 2 GHz bandwidth centered at 230.25 GHz with 30 second integrations. The SMA antenna pairs and the corresponding unprojected baseline lengths are listed above each trace, arranged in order of length. The traces are successively displaced by 1.5 turns in order to make it easier to distinguish between the data points.

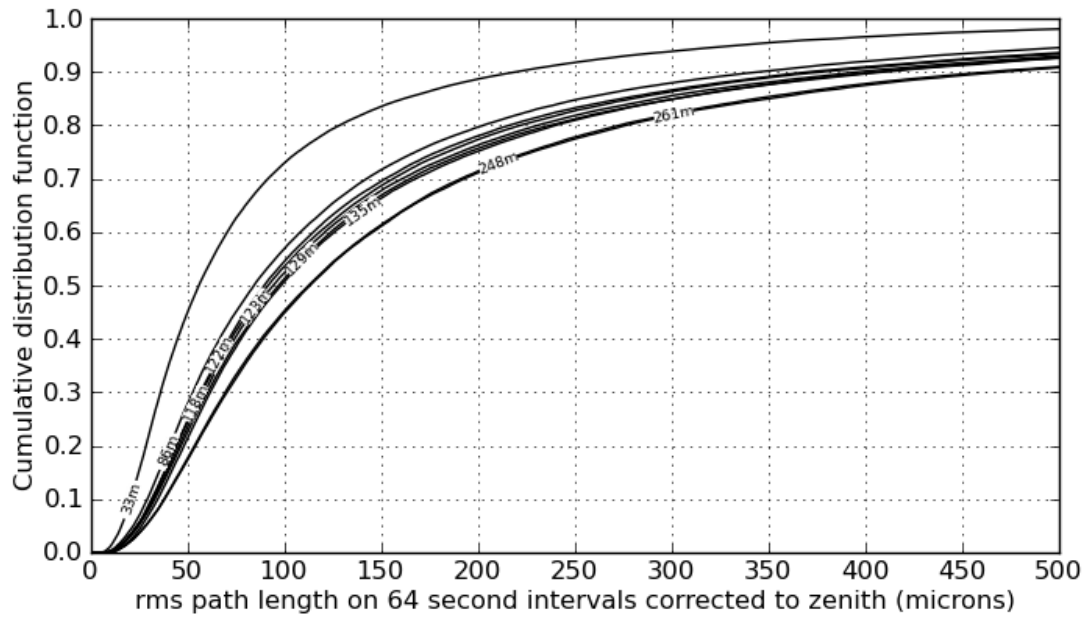


Fig. 8.— The 24-hour cumulative distribution functions of the rms path length (corrected to zenith) on 64 second intervals on nine of the API baselines, labeled by their length ( $B_{\text{proj}}$ ).

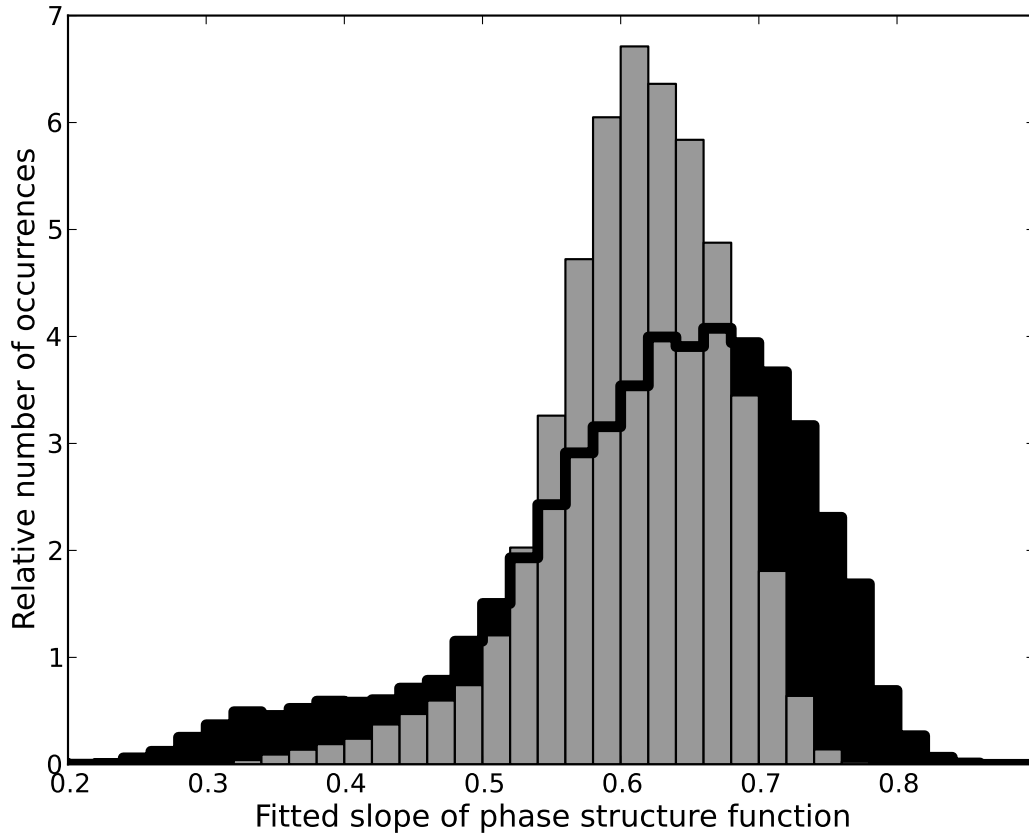


Fig. 9.— Histograms of the fitted slope of the phase structure function ( $\alpha$ ) for the shortest baseline ( $B_{\text{proj}} = 33\text{m}$ ) in black, and the longest baseline ( $B_{\text{proj}} = 261\text{m}$ ) in gray.

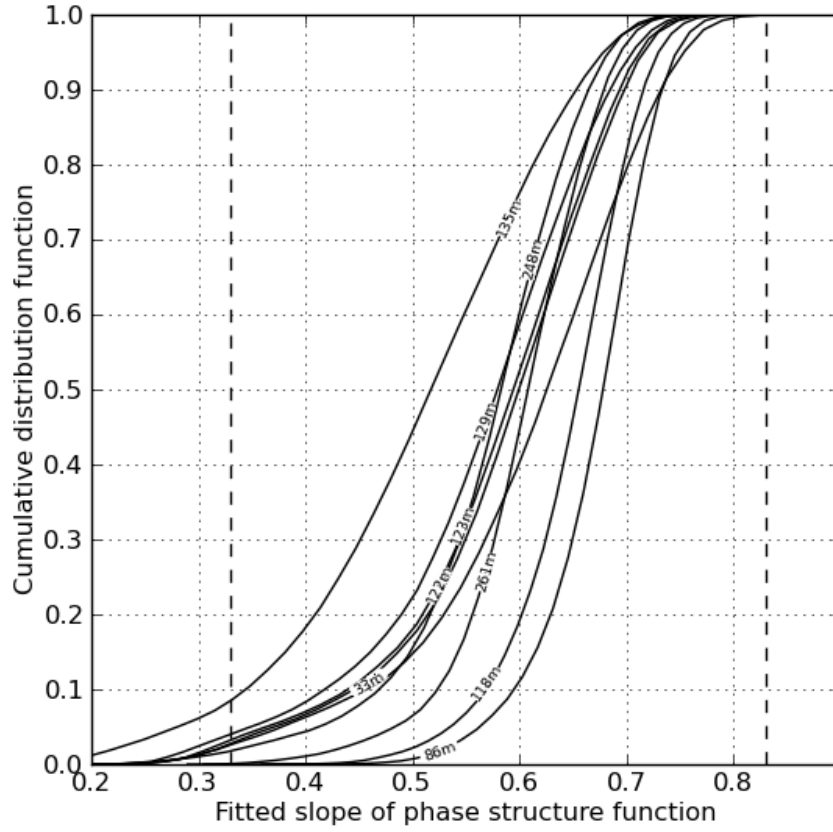


Fig. 10.— Cumulative distribution functions of the fitted slope of the phase structure function  $\alpha$  for nine baselines labeled by  $B_{\text{proj}}$ . The dashed vertical lines mark the expected Kolmogorov values for thin atmospheres (0.33) and thick (0.83) atmospheres.